Research Article | Vol. 27, No. 25 / 9 December 2019 / Optics Express 36100
Optics EXPRESS

Long-distance BOTDA sensing systems using video-BM3D denoising for both static and slowly varying environment

BIWEI WANG,[1] LIANG WANG,[2,*] CHANGYUAN YU,[1,3] AND CHAO LU[1]

[1]*Department of Electronic and Information Engineering, Hong Kong Polytechnic University, Kowloon, Hong Kong*
[2]*National Engineering Laboratory for Next Generation Internet Access System, School of Optics and Electronic Information & Wuhan National Lab for Optoelectronics (WNLO), Huazhong University of Science and Technology, Wuhan 430074, China*
[3]*changyuan.yu@polyu.edu.hk*
[*]*hustwl@hust.edu.cn*

Abstract: In this paper, video block-matching and 3D filtering (VBM3D) denoising has been proposed and experimentally demonstrated for the first time in 100.8 km long-distance Brillouin optical time domain analyzer (BOTDA) sensing system with 2 m spatial resolution. Both experiments under static and slowly varying temperature environment are carried out. A temperature uncertainty of 0.43°C has been achieved with denoising by VBM3D in static temperature measurement. To our knowledge, this is one of the best temperature uncertainty reported for a sensing distance beyond 100 km. The slowly varying temperature at the end of 100.8 km fiber has also been accurately measured. VBM3D exploits both the spatial and temporal correlations of the data for denoising, thus it can significantly reduce the temperature fluctuations and keep the measured values close to the real temperature even if the temperature is temporally changing. We believe it would be useful for the long-distance sensing where the measurand may have temporal evolution in the slowly varying environment.

1. Introduction

Brillouin optical time domain analyzer (BOTDA) sensing systems have attracted much interest over the past three decades due to their unique capability of measuring distributed temperature/strain information with excellent performance [1]. In BOTDA systems, one key issue is the temperature-strain cross sensitivity which makes it difficult to achieve the simultaneous temperature and strain measurement [1]. The solutions up to date include hybrid systems combining Brillouin scattering with Rayleigh/Raman scattering [2–6], using Brillouin frequency shift (BFS) together with the Brillouin peak power or bandwidth or birefringence in the polarization-maintaining fiber (PMF) [7,8], exploiting the BFS of multiple Brillouin peaks in some specialty fibers [9–12]. Besides the temperature-strain cross sensitivity, to achieve long sensing distance beyond 100 km is still a challenge. The signal-to-noise ratio (SNR) is a key parameter which directly limits the measurement accuracy and the sensing distance. Due to the fiber attenuation, the SNR becomes worse at the far end of the fiber under test (FUT), especially for longer sensing distance, which makes the measurement accuracy degrade significantly and hence limits the sensing distance. Although the increase of injected powers of pump and probe light can enhance the SNR in principle, the highest pump and probe powers are limited by the non-local effect [13] and fiber nonlinearities [14], respectively. Therefore, to extend the sensing range beyond 100 km with acceptable spatial resolution and measurement accuracy, some techniques have been proposed, including optical pulse coding [15–21], time/frequency-division multiplexing [22–24], Raman

#379724 https://doi.org/10.1364/OE.27.036100
Journal © 2019 Received 4 Oct 2019; revised 12 Nov 2019; accepted 19 Nov 2019; published 25 Nov 2019

Optics EXPRESS

amplification [18,19,24–28], random fiber laser amplification [25,29], novel probe modulation and scanning [30–32], Brillouin loss configuration [32], and optical chirp chain BOTDA [33]. The works mentioned above with sensing distance beyond 100 km are summarized in Table 1. However, most of the above methods require modifications of the conventional BOTDA setup which make the system more complicated.

Table 1. Summary of previous works in BOTDA with sensing distance beyond 100km

Techniques	Fiber Length	Resolution	BFS Uncertainty
Bipolar pulse coding [15]	100km	2m	0.8MHz
Simplex coding [16]	120km	3m	3.1MHz
Frequency coding [17]	100km	3m	1.5MHz
RZ pulse coding and second-order Raman amplification [18]	100/120km	3/5m	1.5/1.9MHz
Distributed Raman amplification (DRA) and simplex coding [19]	142.2km	5m	1.5MHz
Cyclic coding [20]	164km	1m	3MHz
Bipolar coding [21]	100km	2m	0.9MHz
Time-division multiplexing (TDM) [22]	100km	2m	2MHz
Frequency-division multiplexing (FDM) [23]	150km	2m	1.5MHz
Distributed Raman and Brillouin amplifications, FDM, TDM [24]	150.62km	9m	0.82MHz
Random fiber laser (RFL) based hybrid distributed Raman amplification (H-DRA) [25]	154.4km	5m	1.4MHz
First-order Raman amplification [26]	100km	2m	1.2MHz
Second-order Raman amplification [27]	100km	2m	3MHz
First-order bi-directional Raman amplification [28]	120km	2m	2.1MHz
High-order random fiber laser amplification (RFLA) [29]	175km	8m	2.06MHz
Orthogonally-polarized four-tone probe [30]	104km	2m	5MHz
Novel probe scanning with fixed frequency difference [31]	100km	2m	2.4MHz
Brillouin loss configuration and probe frequency modulation [32]	100km	1m	1MHz
Optical chirp chain (OCC) and pattern recognition [33]	100km	4m	1.3MHz
Non-local means (NLM) image denoising [35]	100km	2m	0.77MHz

On the other hand, image denoising techniques have been used to improve the SNR without the need of modifying the conventional setup, such as non-local means (NLM) and wavelet denoising (WD) [34]. The NLM reduces the noise by using the non-local principle which is based on the high degree of similarity and redundancy contained in the sensing data, while the WD filters the noise by using wavelet transform and wavelet shrinkage. 50km sensing distance with 0.19MHz Brillouin frequency shift (BFS) uncertainty using the 2D WD has been demonstrated [34]. And 100km sensing distance with 0.77MHz BFS uncertainty and 2m spatial resolution has been achieved by using NLM denoising in a conventional BOTDA setup [35], as summarized in Table 1. Recently we have proposed a novel block-matching and 3D filtering (BM3D) image denoising method to enhance the SNR [36]. Since BM3D combines the advantages of NLM and WD, better measurement accuracy with less spatial resolution degradation has been achieved by using BM3D for denoising when compared with those using NLM and WD [36]. However, all these image denoising methods only exploit the data correlation in space domain for denoising, while the temporal correlation of the data is usually ignored. Thus, the 2D image denoising techniques are only suitable for the static environment where the measurand remains unchanged without temporal evolution. Actually, the temporal correlation of the data could also be used together with the spatial correlation for better denoising performance, especially for the slowly

Optics EXPRESS

varying environment when the measurand is changing with time. Using both the temporal and spatial correlation of the data for denoising, 3D video denoising can easily deal with the situations for both the static and slowly varying environment, which denoise the video sequence formed by consecutive measurements of 2D Brillouin gain spectrum (BGS) distribution along the FUT, e.g. NLM video denoising used in the BOTDA with 50km sensing distance [34].

In this paper, we extend the BM3D image denoising to video denoising, i.e. 3D Video-BM3D (VBM3D), in order to add one more temporal dimension and take the dynamical nature of the environment into account. The following manuscript is organized in this manner: Section 2 describes the principle and algorithm of VBM3D. Section 3 discusses the analysis and optimization of primary parameters in the VBM3D algorithm. In this section, experiment results are also included where experiments have been performed for both static and slowly varying temperature environment by using VBM3D for denoising. A BFS uncertainty of 0.44MHz (0.43°C temperature uncertainty) with 100.8km sensing distance and 2m spatial resolution has been achieved for static temperature measurement. The slowly varying temperature at the end of 100.8km FUT has also been successfully measured after denoising by VBM3D. The conclusion is given in Section 4.

2. Working principle of VBM3D denoising

VBM3D is one of the state-of-the-art video denoising methods, which was developed in 2007 for the first time [37]. It reduces the noise by exploiting both spatial and temporal correlation in the signal. In the denoising using VBM3D for BOTDA, each 2D (position-frequency) measurement of Brillouin gain spectrum (BGS) distribution along the FUT by the BOTDA system constructs one frame of a video sequence, e.g. Frame 1, 2, 3 in Fig. 1. And multiple video frames are obtained by consecutive measurements and then are combined together to form the 3D video sequence, which will be denoised by VBM3D. The flowchart of the proposed VBM3D denoising for BOTDA is shown in Fig. 1. Similar to 2D BM3D denoising [38], the VBM3D denoising also includes two repetitive phases and each phase contains three similar steps: grouping, hard-thresholding (in Phase 1)/collaborative Wiener filtering (in Phase 2), and aggregation. The only difference between Phase 1 and Phase 2 is that the collaborative Wiener filtering is used in Phase 2, instead of the hard-thresholding used in Phase 1. The processes of 3 steps in each phase are described briefly as follows:

1) Grouping. In this step, matched blocks “M” which are similar to the reference one “R” are searched by using block-matching method and then stacked together to form a 3D array for each reference block in the video, as shown in Fig. 1. A straightforward approach to extend BM3D to VBM3D is to use fixed-size 3D video search neighborhood. However, using large size will lead to high computation complexity, while using small size will give rise to unsatisfactory grouping and poor denoising results. Thus, the predictive-search block-matching method is used in VBM3D instead of normal block-matching method used in BM3D for grouping. The predictive-search block-matching method includes 2 parts: an exhaustive-search block-matching and a predictive search [37]. And the search range of block-matching in VBM3D is 3D video sequences rather than 2D images as in BM3D.

2) Hard-thresholding/collaborative Wiener filtering. The hard-thresholding and collaborative Wiener filtering are two methods to achieve the 3D transform-domain shrinkage. First, after step 1 in Phase 1, a 3D transform is applied to the 3D array formed in step 1. Second, the hard-thresholding is used in Phase 1 to reduce the noise, and is followed by inverting the 3D transform to produce estimates of all grouped blocks. Then it returns the estimates of the blocks to their original positions. When a complete loop of Phase 1 including steps 1-3 finishes, the collaborative Wiener filtering is used in phase 2 and the steps 1-3 are

Optics EXPRESS

repeated once again to improve the denoising performance further and obtain the final results.

3) Aggregation. After the step 2, a basic (in Phase 1)/final (in Phase 2) estimate of the true video frames is computed by aggregating all of the obtained local estimates using a weighted average.

Fig. 1. Flowchart of the proposed VBM3D denoising for BOTDA. "R" and "M" represent the reference blocks and the matched ones.

The experimental noise originating from all components and equipment in the experiment system, especially the laser, EDFA and PD. And the total experimental noise in the BOTDA system is normally considered to be a Gaussian noise, which could be represented as $\eta(\cdot) \sim \mathcal{N}(0, \sigma^2)$. The observed noisy video is considered as $z(x) = y(x) + \eta(x)$, where y is the true video signal and η represents the noise. Here, $x = (x_1, x_2, t)$ are coordinates in the spatio-temporal 3D domain. The first two components (x_1, x_2) are the spatial coordinates and the third one t is the time (frame) index. The variance σ^2 of noise is assumed a priori known and the standard deviation (SD) σ of noise is set to an estimated value before using the VBM3D algorithm. To elaborate the VBM3D denoising method including 2 phases (each phase contains 3 steps) more concretely, details of the VBM3D algorithm are introduced as following [37]:

1) Phase 1. Obtain a basic estimate using the grouping within the noisy video and the collaborative hard-thresholding.

   a) For each coordinate x, perform: $S_x = PS - BM(Z_x)$, where Z_x denotes a block in the noisy video z at x;

   b) $\hat{Y}_{S_x} = T_{3D}^{-1}(HARD - THR(T_{3D}(Z_{S_x}), \lambda_{3D}\sigma))$, where $\hat{Y}_{S_x}$ is a group of the blockwise estimates $\hat{Y}_{x'}^{x}, \forall x' \in S_x$;

   c) Produce the basic estimate of the whole video $\hat{y}^{basic}$ by aggregation of the blockwise estimates $\hat{Y}_{x'}^{x}$ at each position x, using weighted averaging with $weight(\hat{Y}_{x'}^{x}) = \frac{1}{\sigma^2 N_{har}(x)} W_{2D}$;

2) Phase 2. Obtain the final estimate by grouping within the noisy video and collaborative Wiener filtering that uses the spectra of the corresponding groups from the basic estimate.

   a) For each coordinate x, perform: $S_x = PS - BM(\hat{Y}_x^{basic})$;

   b) $\hat{Y}_{S_x} = T_{3D}^{-1}\left(T_{3D}(Z_{S_x}) \frac{[T_{3D}(\hat{Y}_{S_x}^{basic})]^2}{[T_{3D}(\hat{Y}_{S_x}^{basic})]^2 + \sigma^2}\right)$, where T_{3D} and T_{3D}^{-1} represent 3D transform and inverse 3D transform.

   c) Produce the final estimate of the whole video $\hat{y}^{final}$ by aggregation of $\hat{Y}_{x'}^{x}$, using weighted averaging with $weight(\hat{Y}_{x'}^{x}) = \sigma^{-2} \left\| \frac{[T_{3D}(\hat{Y}_{S_x}^{basic})]^2}{[T_{3D}(\hat{Y}_{S_x}^{basic})]^2 + \sigma^2} \right\|_2^{-2} W_{2D}$, where $\|\cdot\|_2$ denotes $\ell^2 norm$.

Optics EXPRESS

Notation:

- Z_x denotes a block of size $N_1 \times N_1$ in z, whose upper-left corner is at x. Similar notation is used for $\hat{Y}_{x'}^{x}$ and $\hat{Y}_{x}^{basic}$. The former is an estimate for the block located at x', obtained while processing reference block Z_x. And the latter is a block located at x extracted from the basic estimate $\hat{y}^{basic}$.
- $S_x = PS - BM(Z_x)$ performs predictive-search block-matching using Z_x as a reference block, the results of which is the set S_x containing the coordinates of the matched blocks. For Phase 2, the search is performed in the basic estimate instead of in the noisy video.
- Z_{S_x} denotes a group (i.e. a 3D array) formed by stacking together the blocks $Z_{x \in S_x}$. The same notation is used for $\hat{Y}_{S_x}$ and $\hat{Y}_{S_x}^{basic}$. The size of these groups is $N_1 \times N_1 \times |S_x|$.
- $HARD - THR(T_{3D}(Z_{S_x}), \lambda_{3D}\sigma))$ applies hard-thresholding on the coefficients in 3D transform domain using threshold $\lambda_{3D}\sigma$, where λ_{3D} is a fixed threshold parameter. In detail, the hard-thresholding makes two conditional operations on the transform coefficients: when the values of the coefficients are less than the threshold, they are set to zero; and when the values of the coefficients are larger than or equal to the threshold, they are retained.
- $N_{har}(x)$ is the number of nonzero coefficients retained after hard-thresholding $T_{3D}(Z_{S_x})$. Since the DC is always preserved, $N_{har}(x)$>0.
- W_{2D} is a 2D Kaiser window of size $N_1 \times N_1$.

3. Experiment and results

3.1. BOTDA setup

Figure 2 shows the BOTDA experiment setup used to measure BGS distribution along the FUT for VBM3D denoising. The output of a continuous wave (CW) tunable laser working at 1550nm is amplified by an erbium-doped fiber amplifier (EDFA1) and is then split into two branches after filtering. The light at the upper branch is modulated by an electro-optic modulator (EOM1) biased at null point to suppress the optical carrier and driven by a radio frequency (RF) signal generator to provide probe signal. The frequency of the RF source is swept from 10.751GHz to 10.950GHz with 1MHz interval. A variable optical attenuator (VOA) is used to control the probe light power before it enters the fiber under test (FUT). At the lower branch, the CW light is modulated by the EOM2 to generate 20ns pump pulse, corresponding to 2m spatial resolution. The EDFA2 is used to amplify the peak power of the pump pulse and the filter2 is used to remove the amplified spontaneous emission (ASE) noise. The pump peak power and probe power injected into the FUT are 20dBm and -3dBm, respectively, which are below the upper limits to avoid the non-local effect [13] and fiber nonlinearities [14]. The extinction ratio of the pump pulse in our experiment is 40dB. In addition, a polarization scrambler (PS) is used to suppress the polarization dependent noise. After passing through the FUT, the probe signal is amplified by EDFA3 and filtered to remove the higher frequency sideband. Finally, it is detected by a 125 MHz photodetector and collected on an oscilloscope. The sampling rate of 500MSample/s is adopted for data collection on an oscilloscope, which means 0.2m spatial distance between two adjacent data points. A 100.8km long single mode fiber (SMF) is used as the FUT, and its last 196m fiber section is put in the oven to evaluate the measurement accuracy at the far end of the FUT. Another 2.3m loose fiber section is also put inside the oven to verify the experimental spatial resolution. In the experiment for static temperature measurement, 2000 times averaging is adopted. While in the experiment for slowly varying temperature, 200 times averaging is used to not only accelerate the data collection speed but also maintain good signal quality for each group of data.

Optics EXPRESS

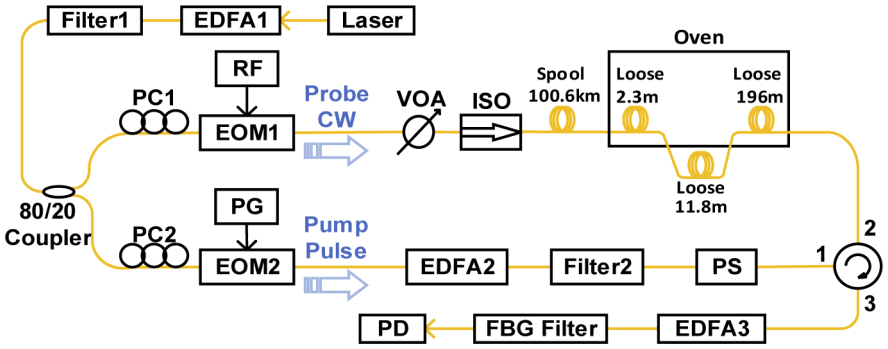

Fig. 2. BOTDA experiment setup. EDFA: erbium-doped fiber amplifier, PC: polarization controller, EOM: electro-optic modulator, RF: radio frequency, PG: pattern generator, VOA: variable optical attenuator, ISO: isolator, FUT: fiber under test, PS: polarization scrambler, FBG: fiber Bragg grating, PD: photodetector.

3.2. *Optimization of VBM3D parameters*

At first, we monitor and analyze the effect of the VBM3D parameters on the denoising performance by experiment. The parameters of VBM3D include the estimated standard deviation (SD) of the experimental noise σ, fixed block size, maximum number of similar blocks, search-window sliding step, search neighborhood range, threshold for the block distance, threshold for the hard-thresholding λ_{3D}. Among these parameters, two primary ones, σ and λ_{3D}, are found to have significant impact on the denoising performance. Thus, we focus on these two parameters and optimize them using experimental data obtained under the condition of static temperature environment (the oven is kept at 60°C). In our experiment, 20 consecutive measurements of BGS distribution along the last 300 m FUT have been taken to form a video sequence, corresponding to a maximum frame number of 20. Then the video is denoised by VBM3D. By using Lorentzian curve fitting (LCF) together with the BFS-temperature coefficient (1.034 MHz/°C) of the FUT, the temperature distribution can be obtained, from which we calculate the temperature uncertainty at the FUT end to evaluate the denoising performance. And we randomly select one frame (15th frame in our case) from these 20 frames for the following performance comparisons. In our tentative trials, we find that by increasing the value of λ_{3D} better temperature uncertainty is observed, but no more improvement is seen when its value is larger than 6. Thus, the value of λ_{3D} is set to be 6 at first and then the value of σ is changing from 0.004 to 0.78 gradually to analyze the denoising performance. The obtained temperature uncertainty at the end of FUT in the 15th frame after denoising by VBM3D (the frame number is set to be 20) is shown in Fig. 3(a). The uncertainty decreases significantly from 8.86°C to 0.43°C while σ increases from 0.004 to 0.20. Then the uncertainty keeps almost unchanged even if σ is still increased. Therefore, to avoid over-denoising and maintain excellent denoising performance, the value of σ is chosen to be 0.20. On the other hand, we keep the value of σ to be 0.20 and gradually increase the value of λ_{3D} from 0.1 to 20 (the frame number is set to be 20). The result is shown in Fig. 3(b), where we can see that the uncertainty decreases significantly and then keeps at the level of 0.43°C when λ_{3D} is larger than 3. We also find that when the frame number is smaller than the maximum value of 20, larger λ_{3D} is needed for the temperature uncertainty to reach a minimum value. To guarantee optimal performance for different frame numbers, we use a little larger value for λ_{3D}, i.e. 6 in our case. Finally, taking the effect of other parameters into account, the values of σ and λ_{3D} are determined to be 0.2 and 6 for the following experiment under both static and slowly varying temperature environment, respectively.

Optics EXPRESS

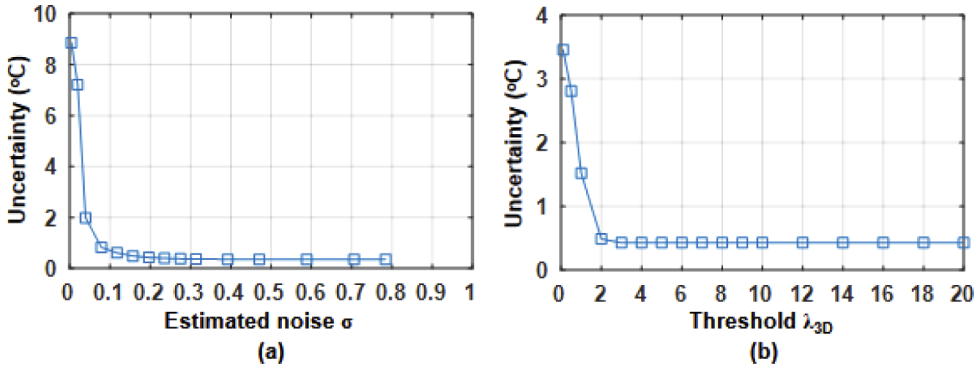

Fig. 3. Temperature uncertainty as a function of (a) estimated SD of noise σ; (b) threshold λ_{3D}.

3.3. VBM3D denoising under static temperature environment

As mentioned above, under the condition of static temperature environment, 20 consecutive measurements of BGS distribution along the last 300 m FUT have been taken to form a video sequence, which means the maximum frame number can be set to be 20. Here we set the frame number to be the maximum value of 20 for denoising at first. Figure 4(a) shows one of the 20 measured BGS distributions along the last 300 m FUT without the denoising by VBM3D, where the two heated FUT sections in the oven cannot be observed due to very low SNR at the FUT end. As a contrast, Fig. 4(b) gives the corresponding BGS distribution after denoising by using VBM3D with a frame number of 20, where an SNR improvement of 13.2 dB (improved from -2.4 dB to 10.8 dB) has been achieved and the two heated sections are clearly observed at the FUT end. Note that the SNR is calculated using 20 m fiber section (101 data points) at the FUT end. And the 15th frame from these 20 frames is randomly selected for analysis and other frames all exhibit similar performance. From Fig. 4, we plot two BGSs at the locations of 100.53 km (at room temperature) and 100.74 km (heated at 60°C) before and after denoising, as shown in Fig. 5, implying that clear BGSs can be reconstructed from the raw data after denoising by VBM3D.

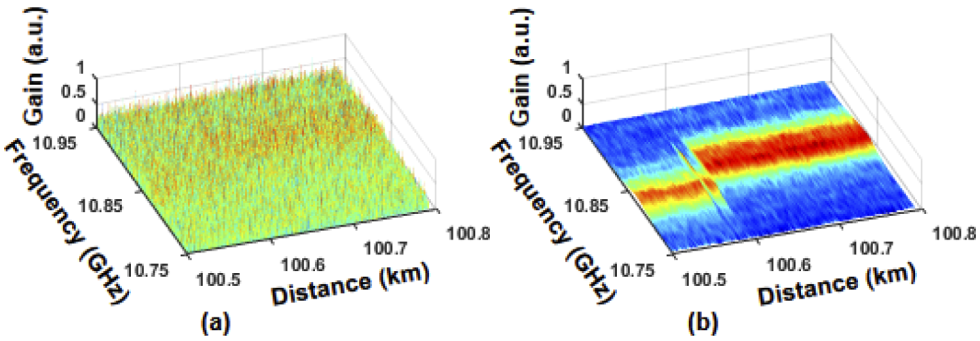

Fig. 4. One of the 20 measured BGS distributions along the last 300 m FUT (a) before denoising; (b) after denoising by using VBM3D with a frame number of 20.

Then, the corresponding temperature distribution is obtained by using LCF together with the BFS-temperature coefficient (1.034 MHz/°C), as shown in Fig. 6(a). It is obvious that the temperature fluctuations are reduced significantly after denoising by VBM3D, and hence the temperatures of the two heated sections at the FUT end are exactly observed. The temperature uncertainty at the far end of FUT is improved from 9.0°C of raw data to 0.43°C (0.44 MHz BFS

Optics EXPRESS

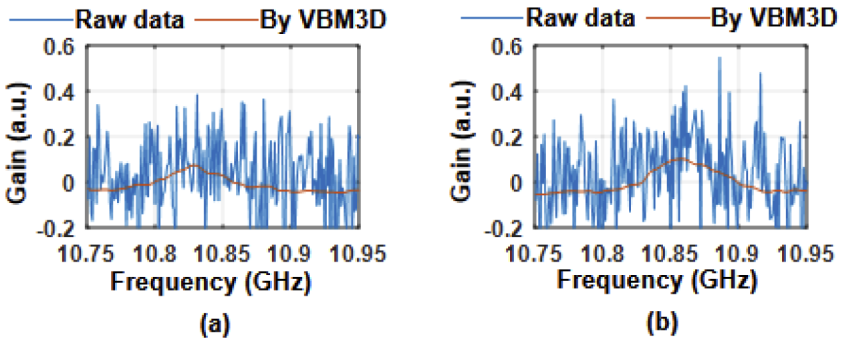

Fig. 5. Two BGSs at the locations of (a) 100.53 km and (b) 100.74 km with/without VBM3D denoising.

uncertainty) after denoising by VBM3D. Figure 6(b) shows the temperature distribution around the 2.3 m heated section, and indicates an experimental spatial resolution of 2.5 m (calculated using the full width at half maximum (FWHM) of the temperature transition section [39]), which has a very small degradation of the spatial resolution after denoising. This result agrees well with our previous work of using 2D BM3D denoising for BOTDA [36], and again shows the advantage of BM3D denoising. It is worth mentioning that in Fig. 4 and Fig. 6 we only present the data along the last 300 m FUT because our oscilloscope does not have enough memory to collect the data along the whole 100.8 km FUT at the sampling rate of 500MSample/s. Since the temperature only changes at the end of FUT and other sections of FUT remain at the room temperature, the data along the last 300 m FUT is good for the demonstration of temperature measurement at the worst SNR.

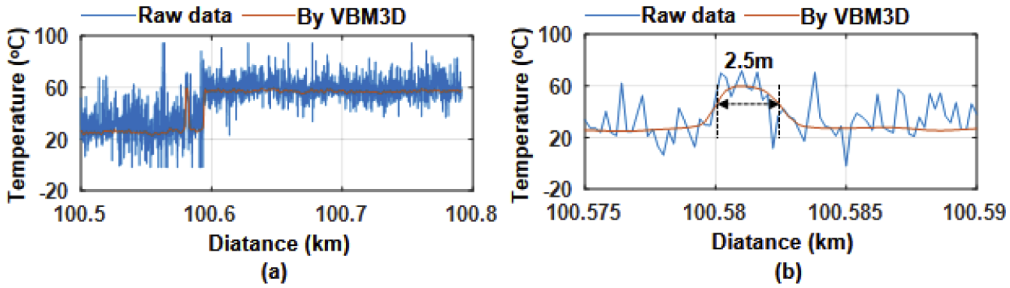

Fig. 6. Temperature distribution before and after denoising by VBM3D (a) along the last 300 m FUT; (b) around the 2.3 m heated section.

It is worth mentioning that the frame number is also a key parameter in VBM3D which determines the search range during block-matching process. Hence the frame number will also affect the denoising performance. In the results of Fig. 4 to Fig. 6, the maximum frame number of 20 is used in VBM3D denoising, which means that the block search range is the whole 20 measurements of the BGS distribution. In order to analyze the denoising performance using VBM3D with different frame numbers, the frame number in VBM3D algorithm is changed. Figure 7 shows the temperature uncertainty at the far end of FUT as a function of the frame number, where the best temperature uncertainty among all of the frames after denoising is adopted. When the frame number is 1, it means there is only one measurement of BGS distribution and VBM3D works in the same way as 2D BM3D. Note that for static temperature environment, 2000 times averaging is adopted for each measurement. The temperature uncertainty obtained by using VBM3D with the frame number of 1, 2, 5, 10, 15 and 20 are 2.13, 1.93, 1.38, 1.12,

Optics EXPRESS

0.52 and 0.43°C, respectively. We can see that the temperature uncertainty becomes better with the increase of the frame number, which indicates the superiority of the VBM3D over the 2D BM3D that VBM3D can make use of not only the spatial correlation within each frame but also the temporal correlation among different frames for denoising. The temporal correlation used in denoising is especially important in the slowly varying temperature measurement, which will be verified in the next section. Moreover, as a comparison, the temperature uncertainty obtained by using linear averaging of multiple measurements is also given in Fig. 7. The temperature uncertainty obtained using linear averaging of 1, 2, 5, 10, 15 and 20 measurements are 9.0, 6.2, 4.1, 3.1, 2.8 and 2.5°C, respectively. It can be seen that the temperature uncertainty obtained by VBM3D is much smaller than that by linear averaging, showing the capability of VBM3D to achieve true data denoising rather than just averaging of redundant data.

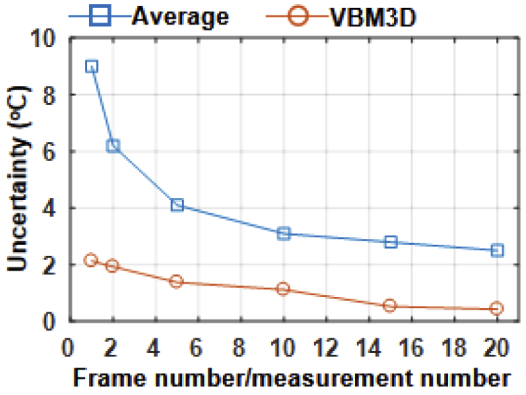

Fig. 7. Temperature uncertainty obtained by using VBM3D and linear averaging as a function of frame number (for VBM3D) or measurement number (for linear averaging).

3.4. VBM3D denoising under slowly varying temperature environment

In this section, we perform the experiment under slowly varying temperature environment, where the temperature inside the oven is slowly changing. At the beginning, the temperature in the oven is kept at 40°C and stabilized for about 40mins. Then, it increases linearly from 40°C to 60°C, which lasts about 140mins. At last, it remains at 60°C for about 45mins. So the whole process of temperature change occupies a time of 225mins, and the process is controlled by a computer connected to the oven. Thus the temperature in oven changes by 20°C within 140mins, corresponding to a temperature change speed of 0.14°C/minute. For each measurement of BGS distribution along the FUT, 200 times averaging is adopted in order to make the data acquisition speed fast enough to sense the temperature change and also maintain good signal quality for such long FUT. The acquisition time of each measurement along FUT costs 3mins, within which the temperature changes by 0.42°C, corresponding to a BFS change of 0.43 MHz (BFS-temperature coefficient of 1.034 MHz/°C). Since 0.43 MHz is even less than one half of the frequency sweeping interval of 1 MHz, the temperature can be regarded as constant within the data acquisition process of each measurement. The measurement starts almost at the same time when the temperature change process begins, and hence the total measurement time is approximately equal to that of temperature change process, i.e. 225mins, during which 76 consecutive measurements of BGS distribution along FUT have been finished. After data collection, they are combined to form a video, which is then denoised by VBM3D with a certain frame number. For example, if the frame number is 10, then the block search range will be adjacent ten measurements and the denoising process will be finished using this block range for all the 76 measurements, as depicted in Fig. 1. Figure 8 shows the temperature as a function of time obtained from a thermometer inside the

Optics EXPRESS

oven (black curve, denoted as real temperature), raw data (red curve) and corresponding data after VBM3D denoising with different frame numbers (1, 2, 5, 10, 15 and 20). Note that for the raw data and those after denoising by VBM3D the measured temperature is the average temperature along the last 196 m FUT in the oven. From Fig. 8, we can see that without denoising the temperature obtained from the raw data has large fluctuations and the values deviate from those measured by the thermometer (i.e. real temperature). While with the denoising by VBM3D both the temperature fluctuations and deviations decrease when the frame number increases from 1 (pink curve) to 15 (blue curve), which clearly indicates that VBM3D can effectively make use of the temporal correlation between each frame to denoise the data under slowly varying temperature environment. However, when the frame number is increased to 20, we find that the temperature after denoising starts to deviate from the real temperature, which may originate from the loss of some useful details of the data due to excessive denoising when using large frame number. The impact of the frame number on the measurement accuracy under slowly varying environment is analyzed quantitatively by calculating the root-mean-square error (RMSE) and uncertainty of the measured temperature values in Fig. 8. The RMSE is calculated by comparing temperatures obtained from 76 measurements (i.e. 76 measured temperature values) with those from the thermometer, which represents how close the measured values are to the real temperature read from the thermometer. The expression of RMSE is given in Eq. (1), where $T^{measured}$ are the temperature values in Fig. 8 obtained from raw data or those after denoising by VBM3D, and T^{ture} are the values read from the thermometer.

$$RMSE = \sqrt{\frac{\sum_{k=1}^{76} (T_k^{measured} - T_k^{true})^2}{N}} \tag{1}$$

While the uncertainty is calculated using the standard deviation (SD) of the temperature values obtained at the FUT end for a randomly selected real temperature, e.g. 53.0°C at the time of 111mins (i.e. the 38th data frame in our case). The RMSE represents the deviations of the measured temperature values from the real ones, while the SD depicts the fluctuations of the measured temperature values. The results of RMSE and SD are given in Fig. 9. Note that frame number equal to zero means the result is obtained from the raw data. From Fig. 9(a) we can see

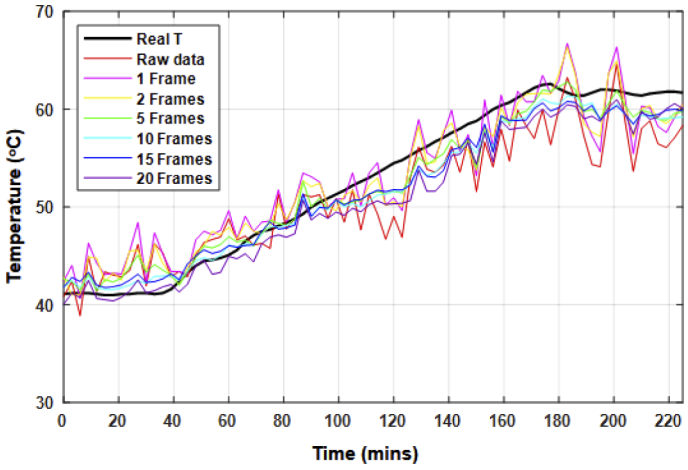

Fig. 8. Temperature as a function of time obtained from a thermometer inside the oven, raw data and data after denoising by VBM3D with different frame numbers (1, 2, 5, 10, 15 and 20). Real T denotes the temperature obtained from the thermometer.

Optics EXPRESS

that the RMSE decreases from 12.86°C to 3.35°C as the frame number increases from 0 to 15. Then it starts to increase when the frame number becomes larger than 15, which agrees well with those in Fig. 8. Since the image/video denoising is achieved at the expense of sacrificing some details in the data [36], more details of the measured data will be lost due to excessive denoising when using larger frame number, resulting in the deviation of the measured temperature from the real temperature and hence the increase of RMSE under larger frame number. On the other hand, the uncertainty has been significantly improved from 21.26°C of raw data to a minimum value of 2.90°C when the frame number is 15, as shown in Fig. 9(b). Similar results of the temperature uncertainty can be obtained for other cases. Taking the case of (58.8°C, 150mins) for example, the temperature uncertainty obtained with frame number of 0, 1, 2, 5, 10, 15 and 20 are 18.48, 8.03, 5.72, 5.41, 3.86, 3.39 and 3.75°C, respectively. The minimum value is also obtained with the frame number of 15.

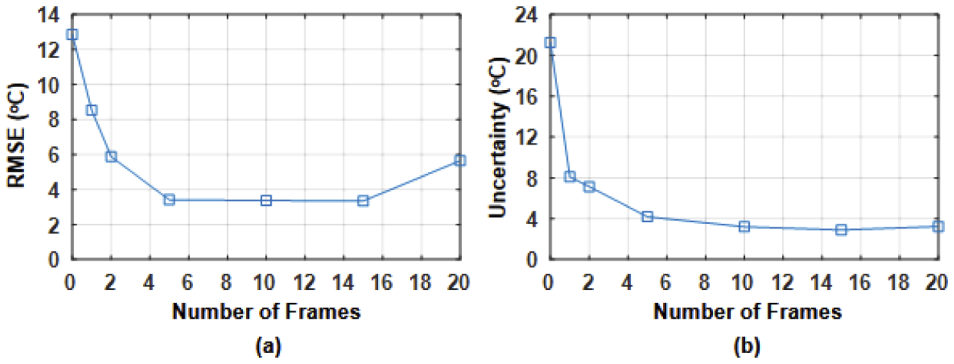

Fig. 9. (a) RMSE and (b) uncertainty of the measured temperatures in Fig. 8 as a function of the frame number.

We also compare the performance of VBM3D and linear averaging under slowly varying temperature environment. Here a frame number of 15 is used for the denoising by VBM3D, while linear averaging of 15 adjacent measurements is adopted for a fair comparison. The results

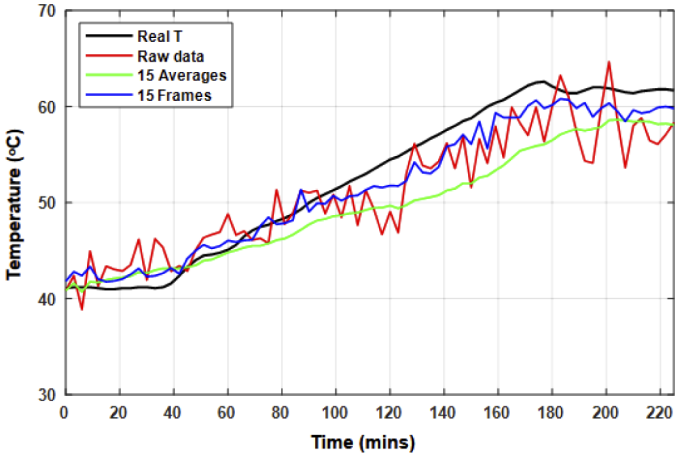

Fig. 10. Comparison of the real temperature by the thermometer (black curve), the measured temperatures by the raw data (red curve), by the data after averaging 15 adjacent measurements (green curve), and by the data denoised using VBM3D with a frame number of 15 (blue curve).

Optics EXPRESS

are plotted in Fig. 10, where the real temperature (black curve), the measured temperatures by the raw data (red curve) and by the data denoised using VBM3D with a frame number of 15 (blue curve) are the same as those in Fig. 8. The temperature as a function of time obtained from the linear averaging is given by the green curve. It can be seen that the temperature from the raw data has large fluctuations due to poor SNR at the end of 100.8km FUT. The linear averaging reduces the fluctuations, but it makes the deviation of the measured temperature from the real temperature become even larger, as depicted by the green curve in Fig. 10. It is because that the linear averaging damages the temporal correlation among the data of adjacent measurements and hence cannot take the slowly varying temperature changing into account. On the other hand, the measured temperature after VBM3D denoising provides not only small fluctuations but also little deviation from the real temperature. As calculated above, the RMSE of the measured temperature by using VBM3D with a frame number of 15 is 3.35°C, compared with RMSE of 12.86°C for raw data and 15.17°C for the data after linear averaging. This significant improvement of measurement accuracy under slowly varying environment proves the advantage of VBM3D which exploits both temporal and spatial correlation for denoising with only little sacrifice of data details even when the environment temperature is slowly changing.

4. Conclusion

We have proposed and experimentally demonstrated the use of 3D VBM3D for denoising in 100 km long-distance BOTDA sensing system with 2 m spatial resolution under both static and slowly varying temperature environment. The video sequence is formed by consecutive measurements of 2D BGS distribution along the FUT, and then is denoised by VBM3D in both time and space domains. Under static temperature environment, the temperature uncertainty of 0.43°C (0.44 MHz BFS uncertainty) at the far end of FUT is achieved. To the best of our knowledge, this is one of the best BFS uncertainty reported for a sensing distance beyond 100 km. On the other hand, the slowly varying temperature has also been successfully measured with a temperature RMSE/uncertainty of 3.35°C/2.90°C. The processing of 1501 (number of sensing points along the last 300 m FUT) × 200 (number of scanned frequencies) ×20 (number of consecutive measurements) data points on our PC with Intel i7-6700k CPU and 16G memory takes 111s. If GPU instead of CPU is used to implement the algorithm, the time can be reduced to 15s [40], and the VBM3D method would be useful in quasi-real-time monitoring scenarios. The reliable denoising performance of the proposed VBM3D method makes it a practical way of improving the measurement accuracy and sensing distance, especially when there is temporal evolution of the measurand under slowly varying environment.

Funding

Research Grants Council, University Grants Committee (CUHK GRF 14204019, PolyU GRF 15211317, 15265816, 15216817); Huazhong University of Science and Technology (startup fund).

Disclosures

The authors declare no conflicts of interest.

References

1. X. Bao and L. Chen, "Recent progress in distributed fiber optic sensors," Sensors **12**(7), 8601–8639 (2012).
2. K. Kishida, C. H. Li, K. Nishiguchi, Y. Yamauchi, A. Guzik, and T. Tsuda, "Hybrid Brillouin-Rayleigh distributed sensing system," *22nd International Conference on Optical Fiber Sensors (OFS2012)*. 8421, 84212G, (2012).
3. K. Kishida, Y. Yamauchi, and A. Guzik, "Study of optical fibers strain-temperature sensitivities using hybrid Brillouin-Rayleigh system," Photonic Sens. **4**(1), 1–11 (2014).

Optics EXPRESS

4. Z. Zhao, Y. Dang, M. Tang, L. Duan, M. Wang, H. Wu, S. Fu, W. Tong, P. P. Shum, and D. Liu, "Spatial-division multiplexed hybrid Raman and Brillouin optical time-domain reflectometry based on multi-core fiber," Opt. Express **24**(22), 25111–25118 (2016).
5. M. Taki, Y. S. Muanenda, I. Toccafondo, A. Signorini, T. Nannipieri, and F. D. Pasquale, "Optimized hybrid Raman/fast-BOTDA sensor for temperature and strain measurements in large infrastructures," IEEE Sens. J. **14**(12), 4297–4304 (2014).
6. Y. Muanenda, C. Oton, T. Nannipieri, A. Signorini, S. Faralli, and F. D. Pasquale, "Hybrid distributed optical fiber sensors for temperature, strain and vibration measurements," *2015 International Conference on Microwave, Optical and Communication Engineering (ICMOCE 2015)*, pp. 1–4 (2015).
7. X. Bao, Q. Yu, and L. Chen, "Simultaneous strain and temperature measurements with polarization-matiaining fibers and their error analysis using distributed Brillouin loss system," Opt. Lett. **29**(12), 1342–1344 (2004).
8. W. Zou, Z. He, and K. Hotate, "Complete discrimination of strain and temperature using Brillouin frequency shift and birefringence in a polarization-maintaining fiber," Opt. Express **17**(3), 1248–1255 (2009).
9. L. Zou, X. Bao, S. Afshar, and L. Chen, "Dependence of the Brillouin frequency shift on strain and temperature in a photonic crystal fiber," Opt. Express **29**(13), 1485–1487 (2004).
10. X. Liu and X. Bao, "Brillouin spectrum in LEAF and simultaneous temperature and strain measurement," J. Lightwave Technol. **30**(8), 1053–1059 (2012).
11. Z. Li, L. Yan, X. Zhang, and W. Pan, "Temperature and strain discrimination in BOTDA fiber sensor by utilizing dispersion compensating fiber," IEEE Sens. J. **18**(17), 7100–7105 (2018).
12. A. Li, Y. Wang, J. Fang, M. Li, B. Y. Kim, and W. Shieh, "Few-mode fiber multi-parameter sensor with distributed temperature and strain discrimination," Opt. Lett. **40**(7), 1488–1491 (2015).
13. A. Dominguez-Lopez, X. Angulo-Vinuesa, A. Lopez-Gil, S. Martin-Lopez, and M. Gonzalez-Herraez, "Non-local effects in dual-probe-sideband Brillouin optical time domain analysis," Opt. Express **23**(8), 10341–10352 (2015).
14. L. Thévenaz, S. F. Mafang, and J. Lin, "Effect of pulse depletion in a Brillouin optical time-domain analysis system," Opt. Express **21**(12), 14017–14035 (2013).
15. M. A. Soto, S. Le Floch, and L. Thévenaz, "Bipolar optical pulse coding for performance enhancement in BOTDA sensors," Opt. Express **21**(14), 16390–16397 (2013).
16. M. A. Soto, G. Bolognini, and F. Di Pasquale, "Long-range simplex-coded BOTDA sensor over 120 km distance employing optical preamplification," Opt. Lett. **36**(2), 232–234 (2011).
17. S. Le Floch, F. Sauser, M. Llera, and E. Rochat, "Novel Brillouin optical time-domain analyzer for extreme sensing range using high-power flat frequency-coded pump pulses," J. Lightwave Technol. **33**(12), 2623–2627 (2015).
18. M. A. Soto, X. Angulo-Vinuesa, S. Martin-Lopez, S. H. Chin, J. D. Ania-Castanon, P. Corredera, E. Rochat, M. Gonzalez-Herraez, and L. Thevenaz, "Extending the real remoteness of long-range Brillouin optical time-domain fiber analyzers," J. Lightwave Technol. **32**(1), 152–162 (2014).
19. X. Jia, Y. Rao, Z. Wang, W. Zhang, C. Yuan, X. Yan, J. Li, H. Wu, Y. Zhu, and F. Peng, "Distributed Raman amplification using ultra-long fiber laser with a ring cavity: characteristics and sensing application," Opt. Express **21**(18), 21208–21217 (2013).
20. H. Iribas, A. Loayssa, F. Sauser, M. Llera, and S. L. Floch, "Cyclic coding for Brillouin optical time-domain analyzers using probe dithering," Opt. Express **25**(8), 8787–8800 (2017).
21. Z. Yang, M. A. Soto, and L. Thévenaz, "Increasing robustness of bipolar pulse coding in Brillouin distributed fiber sensors," Opt. Express **24**(1), 586–597 (2016).
22. Y. Dong, L. Chen, and X. Bao, "Time-division multiplexing-based BOTDA over 100 km sensing length," Opt. Lett. **36**(2), 277–279 (2011).
23. Y. Dong, L. Chen, and X. Bao, "Extending the sensing range of Brillouin optical time-domain analysis combining frequency-division multiplexing and in-line EDFAs," J. Lightwave Technol. **30**(8), 1161–1167 (2012).
24. Y. Fu, Z. Wang, R. Zhu, N. Xue, J. Jiang, C. Lu, B. Zhang, L. Yang, D. Atubga, and Y. Rao, "Ultra-long-distance hybrid BOTDA/φ-OTDR," Sensors **18**(4), 976 (2018).
25. X. H. Jia, J. Y. Rao, C. X. Yuan, J. Li, X. D. Yan, Z. N. Wang, W. L. Zhang, H. Wu, Y. Y. Zhu, and F. Peng, "Hybrid distributed Raman amplification combining random fiber laser based 2nd-order and low-noise LD based 1st-order pumping," Opt. Express **21**(21), 24611–24619 (2013).
26. X. Angulo-Vinuesa, S. Martin-Lopez S, J. Nuño, P. Corredera, J. D. Ania-Castanon, L. Thevenaz, and M. Gonzalez-Herraez, "Raman-assisted Brillouin distributed temperature sensor over 100 km featuring 2 m resolution and 1.2 oC uncertainty," J. Lightwave Technol. **30**(8), 1060–1065 (2012).
27. S. Martin-Lopez, M. Alcon-Camas, F. Rodriguez, P. Corredera, J. D. Ania-Castanon, L. Thevenaz, and M. Gonzalez-Herraez, "Brillouin optical time-domain analysis assisted by second-order Raman amplification," Opt. Express **18**(18), 18769–18778 (2010).
28. M. A. Soto, G. Bolognini, and F. Di Pasquale, "Optimization of long-range BOTDA sensors with high resolution using first-order bi-directional Raman amplification," Opt. Express **19**(5), 4444–4457 (2011).
29. Yun Fu, R. Zhu, B. Han, H. Wu, Y. Rao, C. Lu, and Z. Wang, "175 km repeaterless BOTDA with hybrid high-order random fiber laser amplification," J. Lightwave Technol. **37**(18), 4680–4686 (2019).
30. X. Hong, W. Lin, Z. Yang, S. Wang, and J. Wu, "Brillouin optical time-domain analyzer based on orthogonally-polarized four-tone probe wave," Opt. Express **24**(18), 21046–21058 (2016).

Optics EXPRESS

31. A. Dominguez-Lopez, Z. Yang, M. A. Soto, X. Angulo-Vinuesa, S. Martin-Lopez, L. Thevenaz, and M. Gonzalez-Herraez, "Novel scanning method for distortion-free BOTDA measurements," Opt. Express **24**(10), 10188–10204 (2016).
32. J. J. Mompó, J. Urricelqui, and A. Loayssa, "Brillouin optical time-domain analysis sensor with pump pulse amplification," Opt. Express **24**(12), 12672–12681 (2016).
33. B. Wang, B. Fan, D. Zhou, C. Pang, Y. Li, D. Ba, and Y. Dong, "High-performance optical chirp chain BOTDA by using a pattern recognition algorithm and the differential pulse-width pair technique," Photonics Res. **7**(6), 652–658 (2019).
34. M. A. Soto, J. A. Ramírez, and L. Thévenaz, "Intensifying the response of distributed optical fibre sensors using 2D and 3D image restoration," Nat. Commun. **7**(1), 10870 (2016).
35. M. A. Soto, J. A. Ramírez, and L. Thévenaz, "Optimizing Image Denoising for Long-Range Brillouin Distributed Fiber Sensing," J. Lightwave Technol. **36**(4), 1168–1177 (2018).
36. H. Wu, L. Wang, Z. Zhao, N. Guo, C. Shu, and C. Lu, "Brillouin optical time domain analyzer sensors assisted by advanced image denoising techniques," Opt. Express **26**(5), 5126–5139 (2018).
37. K. Dabov, A. Foi, and K. Egiazarian, "Video denoising by sparse 3D transform-domain collaborative filtering," in *Proc. European Signal Processing Conference (EUSIPCO)* (IEEE, 2007), Poznan, 145–149 (2017).
38. K. Dabov, A. Foi, V. Katkovnik, and K. Egiazarian, "Image denoising by sparse 3-D transform-domain collaborative filtering," IEEE Trans. on Image Process. **16**(8), 2080–2095 (2007).
39. Y. Dong, H. Zhang, L. Chen, and X. Bao, "2 cm spatial-resolution and 2 km range Brillouin optical fiber sensor using a transient differential pulse pair," Appl. Opt. **51**(9), 1229–1235 (2012).
40. S. Sarjanoja, J. Boutellier, and J. Hannuksela, "BM3D image denoising using heterogeneous computing platforms," in *Conf. on Design and Architectures for Signal and Image Processing* (DASIP 2015), pp. 4159–4167 (2015).